

MIT Open Access Articles

*The R -Process Alliance: Discovery of a Low- α , r -
process-enhanced Metal-poor Star in the Galactic Halo*

The MIT Faculty has made this article openly available. **Please share**
how this access benefits you. Your story matters.

Citation: Sakari, Charli M. et al. "The R -Process Alliance: Discovery of a Low- α , r -process-enhanced Metal-poor Star in the Galactic Halo." *Astrophysical Journal*, 874, 2 (April 2019): 148 © 2019 The Author(s)

As Published: 10.3847/1538-4357/AB0C02

Publisher: American Astronomical Society

Persistent URL: <https://hdl.handle.net/1721.1/128687>

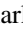
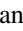



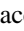

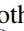
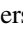







Version: Final published version: final published article, as it appeared in a journal, conference proceedings, or other formally published context

Terms of Use: Article is made available in accordance with the publisher's policy and may be subject to US copyright law. Please refer to the publisher's site for terms of use.





The *R*-Process Alliance: Discovery of a Low- α , *r*-process-enhanced Metal-poor Star in the Galactic Halo

Charli M. Sakari¹ , Ian U. Roederer^{2,3} , Vinicius M. Placco^{3,4} , Timothy C. Beers^{3,4} , Rana Ezzeddine^{3,5} , Anna Frebel^{3,5} , Terese Hansen⁶ , Christopher Sneden⁷ , John J. Cowan⁸, George Wallerstein¹, Elizabeth M. Farrell¹, Kim A. Venn⁹ , Gal Matijević¹⁰, Rosemary F. G. Wyse¹¹, Joss Bland-Hawthorn^{12,13} , Cristina Chiappini¹⁰, Kenneth C. Freeman¹⁴ , Brad K. Gibson¹⁵ , Eva K. Grebel¹⁶, Amina Helmi¹⁷ , Georges Kordopatis¹⁸ , Andrea Kunder¹⁹ , Julio Navarro⁹, Warren Reid^{20,21}, George Seabroke²², Matthias Steinmetz¹⁰ , and Fred Watson²³

¹Department of Astronomy, University of Washington, Seattle WA 98195-1580, USA; sakaricm@u.washington.edu

²Department of Astronomy, University of Michigan, 1085 S. University Ave., Ann Arbor, MI 48109, USA

³Joint Institute for Nuclear Astrophysics Center for the Evolution of the Elements (JINA-CEE), USA

⁴Department of Physics, University of Notre Dame, Notre Dame, IN 46556, USA

⁵Department of Physics and Kavli Institute for Astrophysics and Space Research, Massachusetts Institute of Technology, Cambridge, MA 02139, USA

⁶Mitchell Institute for Fundamental Physics and Astronomy and Department of Physics and Astronomy, Texas A&M University, College Station, TX 77843-4242, USA

⁷Department of Astronomy and McDonald Observatory, The University of Texas, Austin, TX 7 8712, USA

⁸Homer L. Dodge Department of Physics and Astronomy, University of Oklahoma, Norman, OK 73019, USA

⁹Department of Physics and Astronomy, University of Victoria, Victoria, BC, Canada

¹⁰Leibniz Institut für Astrophysik Potsdam (AIP), An der Sternwarte 16, D-14482 Potsdam, Germany

¹¹Physics and Astronomy Department, Johns Hopkins University, 3400 North Charles Street, Baltimore, MD 21218, USA

¹²Sydney Institute for Astronomy, School of Physics A28, University of Sydney, NSW 2006, Australia

¹³ARC Centre of Excellence for All Sky Astrophysics (ASTRO-3D), Australia

¹⁴Research School of Astronomy & Astrophysics, The Australian National University, Cotter Road, Canberra, ACT 2611, Australia

¹⁵E.A. Milne Centre for Astrophysics, University of Hull, Hull, HU6 7RX, UK

¹⁶Astronomisches Rechen-Institut, Zentrum für Astronomie der Universität Heidelberg, Mönchhofstr. 12–14, D-69120 Heidelberg, Germany

¹⁷Kapteyn Astronomical Institute, University of Groningen, P.O. Box 800, NL-9700 AV Groningen, The Netherlands

¹⁸Université Côte d’Azur, Observatoire de la Côte d’Azur, CNRS, Laboratoire Lagrange, France

¹⁹Saint Martin’s University, 5000 Abbey Way SE, Lacey, WA 98503, USA

²⁰Department of Physics and Astronomy, Macquarie University, Sydney, NSW 2109, Australia

²¹Western Sydney University, Locked bag 1797, Penrith South, NSW 2751, Australia

²²Mullard Space Science Laboratory, University College London, Holmbury St Mary, Dorking, RH5 6NT, UK

²³Department of Industry, Innovation and Science, 105 Delhi Road, North Ryde, NSW 2113, Australia

Received 2018 November 15; revised 2019 February 26; accepted 2019 March 1; published 2019 April 2

Abstract

A new moderately *r*-process-enhanced metal-poor star, RAVE J093730.5–062655, has been identified in the Milky Way halo as part of an ongoing survey by the *R*-Process Alliance. The temperature and surface gravity indicate that J0937–0626 is likely a horizontal branch star. At $[\text{Fe}/\text{H}] = -1.86$, J0937–0626 is found to have subsolar $[\text{X}/\text{Fe}]$ ratios for nearly every light, α , and Fe-peak element. The low $[\alpha/\text{Fe}]$ ratios can be explained by an ~ 0.6 dex excess of Fe; J0937–0626 is therefore similar to the subclass of “iron-enhanced” metal-poor stars. A comparison with Milky Way field stars at $[\text{Fe}/\text{H}] = -2.5$ suggests that J0937–0626 was enriched in material from an event, possibly a Type Ia supernova, that created a significant amount of Cr, Mn, Fe, and Ni and smaller amounts of Ca, Sc, Ti, and Zn. The *r*-process enhancement of J0937–0626 is likely due to a separate event, which suggests that its birth environment was highly enriched in *r*-process elements. The kinematics of J0937–0626, based on *Gaia* DR2 data, indicate a retrograde orbit in the Milky Way halo; J0937–0626 was therefore likely accreted from a dwarf galaxy that had significant *r*-process enrichment.

Key words: Galaxy: formation – stars: abundances – stars: atmospheres – stars: fundamental parameters – stars: individual (RAVE J093730.5–062655)

Supporting material: machine-readable table

1. Introduction

The advent of large surveys has provided insight into the formation and evolution of the Milky Way (MW) and its satellites, particularly the nucleosynthesis of the elements and chemical evolution in galaxies of different masses. Many open questions remain, however, including the astrophysical site for the creation of the heaviest elements in the universe. These elements are created by the rapid (*r*-) neutron capture process; suggestions that *r*-process nucleosynthesis could occur during a neutron star merger (Lattimer & Schramm 1974; Rosswog et al. 2014; Lippuner et al. 2017) have now been confirmed

through observations of GW170817 (Abbott et al. 2017; Chornock et al. 2017; Drout et al. 2017; Shappee et al. 2017). However, core-collapse supernovae from strongly magnetic stars (the so-called “jet-supernovae”) may also be a viable site of the *r*-process (e.g., Winteler et al. 2012; Cescutti et al. 2015; Côté et al. 2018). One of the most useful sites for probing the environments, yields, and occurrence rates for *r*-process nucleosynthesis are the *r*-process-enhanced metal-poor stars, which retain a relatively pure *r*-process signature and whose spectra are not overly contaminated from metal lines.

A new collaboration, the *R*-Process Alliance (RPA), has begun a campaign to identify more of these *r*-process-enhanced

metal-poor stars (with $[\text{Ba}/\text{Eu}] < 0$), with the ultimate goal of constraining the site(s) of the r -process across cosmic time. Initial results from the Northern and Southern Hemisphere surveys (Hansen et al. 2018; Sakari et al. 2018a, plus additional papers from Placco et al. 2017; Cain et al. 2018; Gull et al. 2018; Holmbeck et al. 2018; Roederer et al. 2018b; Sakari et al. 2018b) have identified many more of these stars, including 18 new highly enhanced r -II stars (with $[\text{Eu}/\text{Fe}] > +1.0$) and 101 new moderately enhanced r -I stars (with $+0.3 \leq [\text{Eu}/\text{Fe}] \leq +1.0$), according to the classifications from Beers & Christlieb (2005). These new discoveries enable the r -process-enhanced metal-poor stars to be studied as stellar populations, so that their chemical and kinematic properties can be assessed as a whole.

Though they serve as useful laboratories for studying the r -process, it is still not known how or where r -process-enhanced stars form, including how they have retained such a strong r -process signal without being significantly diluted by the nucleosynthetic products of other stars (e.g., core collapse supernovae). One theory is that the r -process-enhanced stars form in the lower-mass ultra-faint dwarfs which are later accreted into the MW halo. This framework is supported by both observations and simulations: r -process-enhanced stars have been found in ultra-faint dwarfs, notably Reticulum II (Ji et al. 2016; Roederer et al. 2016), while simulations suggest that low-mass dwarf galaxies are capable of retaining the ejecta from an r -process nucleosynthetic event (e.g., Bland-Hawthorn et al. 2015; Beniamini et al. 2018). In addition, the r -process-enhanced stars are also predominantly old (e.g., Placco et al. 2017; Holmbeck et al. 2018; Sakari et al. 2018a; Valentini et al. 2018), and simulations indicate that many of the oldest stars in the MW halo may have been accreted (e.g., Steinmetz & Müller 1994; Brook et al. 2007, 2012; El-Badry et al. 2018).

Another convincing piece of evidence for an extragalactic origin for the r -process-enhanced stars comes from kinematics. Several r -II stars have orbits consistent with accretion from a satellite (Roederer et al. 2018a), while many of the highly enhanced r -II and r -I stars have retrograde orbits in the MW halo which indicate an extragalactic origin (e.g., Sakari et al. 2018a). An increased number of r -I and r -II stars, combined with increasingly better data from *Gaia* (Gaia Collaboration et al. 2016), will enable detailed orbits and more subgroups to be identified, as was done in Koppelman et al. (2018) and Roederer et al. (2018a).

Some dwarf galaxy stars can also be identified chemically, as a result of differing chemical evolution in massive and low-mass galaxies (see, e.g., Tolstoy et al. 2009). This is generally only possible for intermediate-metallicity stars that have formed after several previous generations of stars (i.e., after enough time has passed to allow chemical evolution to proceed differently in the low-mass environment). This also requires that the accreted dwarf galaxy experienced extended epochs of star formation, rather than a single burst (see Webster et al. 2015 for evidence that this is possible, even in the lowest-mass ultra-faint dwarfs). The majority of metal-poor stars are unlikely to show the chemical signatures of more metal-rich dwarf galaxy stars. A few exceptions have been identified in the MW halo, notably the class of “Fe-enhanced” metal-poor stars which show low $[\text{X}/\text{Fe}]$ ratios at $[\text{Fe}/\text{H}] < -1$ (e.g., Yong et al. 2013); generally, however, these stars are fairly rare. Until now, none of these stars in the MW halo have been r -process enhanced.

This paper reports the discovery of an r -process-enhanced metal-poor star that exhibits the typical chemical signatures of dwarf galaxy stars (notably low $[\alpha/\text{Fe}]$ ratios). Section 2 describes the observations, data reduction, and atmospheric parameters of this star, while Section 3 presents the abundances. The implications of these abundances, the kinematics, and comparisons with other MW halo stars and dwarf galaxy stars are discussed in Section 4.

2. Observations, Data Reduction, and Atmospheric Parameters

J0937–0626 was identified as a metal-poor star in Data Release 4 of the Radial Velocity Experiment (RAVE; Steinmetz et al. 2006; Kordopatis et al. 2013) and the subsequent re-analysis by Matijević et al. (2017). It was then targeted for a medium-resolution optical analysis by Placco et al. (2018). J0937–0626 was then observed at high spectral resolution in 2016 and 2017 using the Astrophysical Research Consortium (ARC) 3.5 m telescope at Apache Point Observatory, as part of the Northern Hemisphere survey of the RPA (Sakari et al. 2018a). The ARC Echelle Spectrograph was used in its default mode, leading to a spectral resolution of $R \sim 31,500$ and coverage of nearly the full optical range, from 3800 to 10400 Å. The exposure times were selected to ensure high signal-to-noise ratios (S/N) in the red and the blue, as shown in Table 1. The data were reduced in the Image Reduction and Analysis Facility program (IRAF)²⁴ using standard techniques, as described in Sakari et al. (2018a). The heliocentric radial velocity was found by cross-correlating the spectrum with a high-resolution, high-S/N spectrum of Arcturus (Hinkle et al. 2003). The radial velocity is in excellent agreement with the value from RAVE DR5 (see Table 1).

Equivalent widths (EWs) of Fe I and Fe II lines from Fulbright et al. (2006), Venn et al. (2012), and McWilliam et al. (2013) were found using the automated program DAOSPEC (Stetson & Pancino 2008). Fe abundances were then determined using the 2017 version of MOOG (Snedden 1973), with an appropriate treatment of scattering (Sobeck et al. 2011).²⁵ The $\langle 3D \rangle$, non-Local Thermodynamic Equilibrium (NLTE) corrections from Amarsi et al. (2016) were applied to each Fe I line, as discussed in Sakari et al. (2018a). The temperature and microturbulent velocity of J0937–0626 were determined by removing trends in the NLTE Fe I abundances with wavelength, reduced EW, and excitation potential (see Figure 1); the surface gravity was found by forcing agreement between NLTE Fe I and Fe II abundances. The final adopted parameters are listed in Table 1, along with the LTE parameters and the parameters derived with the 1D NLTE corrections of Ezzeddine et al. (2017; also see Ezzeddine et al. 2016 and Sakari et al. 2018a for more details). The Ezzeddine et al. corrections lead to similar parameters as the Amarsi et al. $\langle 3D \rangle$ NLTE corrections. The largest effect of the NLTE corrections to the Fe I lines is to raise the surface gravity and the $[\text{Fe}/\text{H}]$ over the LTE values.

Schuster et al. (2004) and Beers et al. (2007) obtained photometry of J0937–0626, finding colors that are consistent with the spectroscopic parameters derived here.

²⁴ IRAF is distributed by the National Optical Astronomy Observatory, which is operated by the Association of Universities for Research in Astronomy, Inc., under cooperative agreement with the National Science Foundation.

²⁵ <https://github.com/alexji/moog17scat>

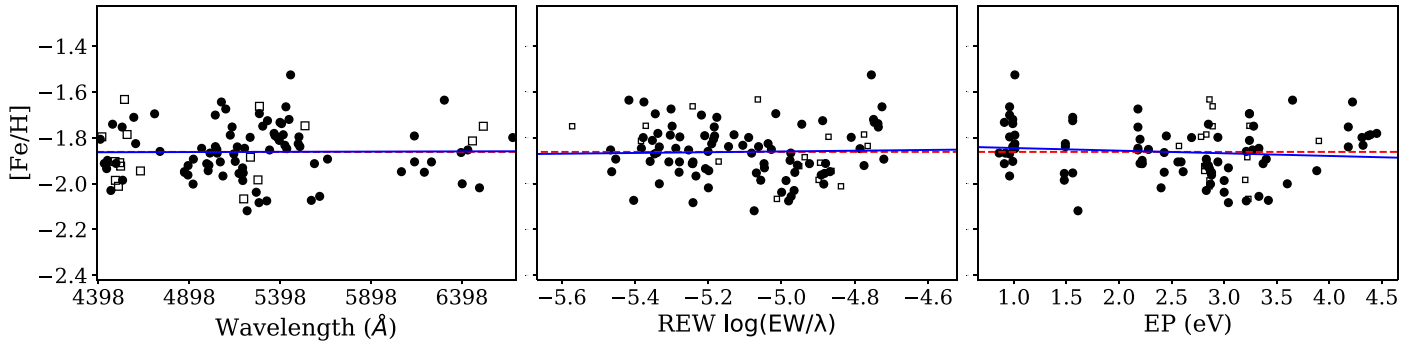


Figure 1. Trends in $[\text{Fe}/\text{H}]$ for Fe I and Fe II lines (filled circles and open squares, respectively) in J0937–0626. The dashed red line shows the average Fe I abundance, while the solid blue lines show the least-squares fits to the Fe I lines.

Table 1
Target Information

Parameter	Value	Notes
ID	RAVE J093730.5–062655	Other IDs: TYC 4900-1967-1, BS 17576-0027, 2MASS J09373053-0626551
R.A. (J2000)	09:37:30.54	...
Decl. (J2000)	−06:26:55.0	...
V	11.81	...
K	10.13	...
$E(B - V)$	0.0266	Average value from Schlafly & Finkbeiner (2011) maps
d (kpc)	$2.342^{+0.230}_{-0.192}$	Inverse parallax distance
	$2.149^{+0.190}_{-0.163}$	Bailer-Jones et al. (2018)
M_V	-0.120 ± 0.18	Calculated from the inverse parallax distance
	0.067 ± 0.18	Calculated from the Bailer-Jones et al. (2018) distance
Observation dates	2016 Jan 28, Feb 11, 2017 Mar 2	Seeing = 0.9, 1.09, 1''12
Exposure time (s)	3240	...
S/N, 4400 Å	100	Per pixel; there are 2.5 pixels per resolution element
S/N, 6500 Å	170	Per pixel; there are 2.5 pixels per resolution element
v_{helio} (km s ^{−1})	268.8 ± 1.0	This work
	268.436 ± 1.297	RAVE DR5
T_{eff} (K)	5875 ± 55^a	Spectroscopic, with <3D> NLTE correction; this work
	5875 ± 55	Spectroscopic, LTE; this work
	5850 ± 50	Spectroscopic, with 1D NLTE Ezzeddine et al. (2017) corrections; this work
	6091	Spectroscopic, Placco et al. (2018)
	5667.31 ± 214	Spectroscopic, RAVE DR5
	5606	Photometric, Ramírez & Meléndez (2005) calibration
	5752	Photometric, Casagrande et al. (2010) calibration
$\log g$	2.61 ± 0.16^a	Spectroscopic, this work
	2.31 ± 0.16	Spectroscopic, LTE; this work
	2.70 ± 0.20	Spectroscopic, with 1D NLTE Ezzeddine et al. (2017) corrections; this work
	2.52	Spectroscopic, Placco et al. (2018)
	2.81 ± 0.48	Spectroscopic, RAVE DR5
ξ (km/s)	2.09 ± 0.25^a	This work
	2.14 ± 0.25	Spectroscopic, LTE; this work
	2.20 ± 0.20	Spectroscopic, with 1D NLTE Ezzeddine et al. (2017) corrections; this work
[M/H]	−2.04	RAVE DR5
[Fe/H]	-1.86 ± 0.02^a	This work
	-2.03 ± 0.02	Spectroscopic, LTE; this work
	-1.89 ± 0.15	Spectroscopic, with 1D NLTE Ezzeddine et al. (2017) corrections; this work
	−1.70	Placco et al. (2018)
[C/Fe]	-0.55 ± 0.40^a	Measured value, this work
	$\sim +0.1$	“Natal” value, calculated with the evolutionary corrections of Placco et al. (2014) ^b
	+0.38	Measured value, Placco et al. (2018)

Notes.

^a The bold values show the final spectroscopic values adopted for the abundance analysis.

^b This correction assumes that the star is a horizontal branch star, and therefore has the same level of C depletion as a tip of the red giant branch star.

Schuster et al. (2004) classified J0937–0626 as a “red-horizontal-branch-asymptotic-giant-branch transition” star, while Beers et al. (2007) found that it was displaced from the

metal-poor main sequence, potentially as a result of its lower surface gravity. Indeed, the spectroscopic parameters for J0937–0626 place it in the expected region for old, moderately

metal-poor HB stars. The spectroscopic temperature is also in agreement with the photometric analysis by Munari et al. (2014) and the spectroscopic RAVE DR5 value (Kunder et al. 2017), while the temperature, surface gravity, and metallicity are in agreement with the medium-resolution analysis of Placco et al. (2018). *Gaia* has provided a parallax for J0937–0626 in Data Release 2 (Gaia Collaboration et al. 2016, 2018), which gives a distance; Bailer-Jones et al. (2018) also provide a statistically determined distance (see Table 1). These distances, combined with the $E(B - V)$ from the Schlafly & Finkbeiner (2011) reddening maps, indicate that J0937–0626 likely has an absolute magnitude of $M_V = -0.120 \pm 0.18$ (with the inverse parallax distance) or $M_V = 0.067 \pm 0.18$ (with the Bailer-Jones et al. 2018 distance). These magnitudes are both consistent with J0937–0626 being a red horizontal branch star.

Very few red horizontal branch stars have been observed by the RPA; the targets are mainly red giant branch stars. However, though J0937–0626 may be a horizontal branch star, its abundances should reflect the composition of typical MW stars (with the exception of C; see the discussion in Section 4.2 and Figure 2 in Roederer et al. 2018b). Also note that its atmospheric parameters place J0937–0626 within the extent of the NLTE grid from Amarsi et al. (2016, see their Table 2). To further confirm that the NLTE corrections are appropriate for a red horizontal branch star, the more metal-rich r -II star HD 222925 from Roederer et al. (2018b) was re-analyzed. Its parameters with the <3D> NLTE Amarsi et al. corrections ($T_{\text{eff}} = 5625$ K, $\log g = 2.3$, $\xi = 1.75$ km s $^{-1}$, and $[\text{Fe I}/\text{H}] = -1.44$) agree with the photometric parameters from Roederer et al. ($T_{\text{eff}} = 5636$ K, $\log g = 2.54$) and are higher than the spectroscopic parameters ($\xi = 2.20$ km s $^{-1}$, and $[\text{Fe I}/\text{H}] = -1.58$, though note than Roederer et al. find $[\text{Fe II}/\text{H}] = -1.47$). The offsets in the metallicity and microturbulent velocity are consistent with the general trends found in LTE versus NLTE comparison (e.g., Amarsi et al. 2016). However, in HD 222925 these atmospheric parameter offsets only lead to small differences in the $[\text{X}/\text{Fe}]$ ratios ($\lesssim 0.1$ dex); this indicates that the <3D> NLTE Fe I corrections produce reasonable results for red horizontal branch stars.

Carbon abundances were found by synthesizing the CH G-band region at 4312 Å. J0937–0626 is found to have a subsolar $[\text{C}/\text{Fe}] = -0.55 \pm 0.40$, a reasonably low value given its advanced evolutionary state. Taking the evolutionary corrections of Placco et al. (2014) into account, the “natal” carbon abundance was likely higher, at $[\text{C}/\text{Fe}] \sim 0.1$. J0937–0626 is not (and never was) a carbon-enhanced metal-poor star.

3. Detailed Abundances

Abundances of Fe, Ca, Sc, Ti, Cr, Mn, Co, and Ni were determined from EWs; all other elements were determined from spectrum syntheses. The lines for the EW analyses are from the line lists of Fulbright et al. (2006, 2007) and McWilliam et al. (2013). Corrections for hyperfine structure and (if necessary) isotopic splitting were included for Sc, V, Mn, and Co, using the data from the Kurucz database²⁶ and McWilliam et al. (2013). The spectrum synthesis line lists were generated with the `linemake` code.²⁷ Hyperfine structure, isotopic splitting, and molecular lines from CH, C₂, and CN were included in the synthetic spectrum line lists. All $[\text{X}/\text{H}]$

Table 2
Line Equivalent Widths or Abundances

Element	Wavelength (Å)	EP (eV)	$\log gf$	EW (mÅ)	$\log \epsilon$	Flag ^a
Na I	5895.92	0.00	-0.180	...	4.13	SYN
Mg I	4167.28	4.34	-0.745	...	5.56	SYN
Mg I	4703.00	4.34	-0.670	...	5.46	SYN
Mg I	5528.41	4.34	-0.480	...	5.44	SYN
Al I	3944.00	0.00	-0.640	...	3.17	SYN
Al I	3961.52	0.01	-0.340	...	3.24	SYN
Si I	3905.52	1.91	-1.090	...	5.20	SYN
Ca I	4283.01	1.89	-0.220	35.7	...	EW
Ca I	4289.37	1.88	-0.300	29.7	...	EW
Ca I	4302.54	1.90	0.275	63.1	...	EW

Note.

^a A flag of “SYN” indicates that the abundance was determined via spectrum synthesis; in this case, a $\log \epsilon$ abundance is given. “EW” indicates that an equivalent width analysis was performed, and the measured EW is given instead of an abundance.

(This table is available in its entirety in machine-readable form.)

ratios were calculated line-by-line, where the solar abundance has been determined from the Kurucz solar spectrum²⁸ if the lines are sufficiently weak and unblended, using the same atomic data; otherwise, the Asplund et al. (2009) solar values are adopted. Note that unlike Sakari et al. (2018a), a differential analysis has not been utilized, because there is no suitable standard star in this metallicity range.

Table 2 shows the line-by-line EWs or, for lines whose abundances were derived from spectrum syntheses, abundances. Table 3 shows the final mean abundances. For the EW-based abundances, the random errors represent the line-to-line dispersion, with a minimum error in a single line of 0.05–0.1 dex, depending on the strength of the line and S/N; for abundances that were determined via spectrum syntheses, the random errors are based on the quality of the syntheses. Table 3 also shows the total error, which is a quadrature sum of the random error and the systematic error due to uncertainties in the atmospheric parameters. The systematic errors were determined from the variances and covariances of the atmospheric parameters, according to the techniques outlined in McWilliam et al. (2013) and Sakari et al. (2018a). Table 3 also provides the abundance offsets that occur if LTE parameters are adopted. The offsets are all $\lesssim 0.2$ dex; all $[\text{X}/\text{Fe}]$ ratios relative to Fe II are negligible. These offsets reflect the abundance sensitivities to differences in $\log g$, microturbulent velocity, and $[\text{Fe I}/\text{H}]$. NLTE corrections were not applied to elements other than Fe I; significant NLTE sensitivities are generally noted below.

3.1. Light Elements: Na and Al

The Na abundance was determined from a synthesis of the 5895 Å Na I line (the 5889 Å line is too strong), indicating a slightly subsolar $[\text{Na}/\text{Fe}]$ ratio. The Al I lines at 3944 and 3961 Å yield a significantly subsolar $[\text{Al}/\text{Fe}] = -1.40 \pm 0.06$. Table 3 shows the LTE abundances, but both the Na and Al lines likely suffer from NLTE effects. The *INSPECT* database²⁹ (Lind et al. 2011) indicates that the 5895 Å Na I line should have an NLTE

²⁶ <http://kurucz.harvard.edu/linelists.html>

²⁷ <https://github.com/vmplacco/linemake>

²⁸ <http://kurucz.harvard.edu/Sun.html>

²⁹ <http://inspect-stars.com/>

Table 3
Mean Abundances and Uncertainties

Element	N	$\log \epsilon$	σ_{random}	$\sigma_{\text{Tot}}^{\text{a}}$	$[X/\text{Fe}]^{\text{b}}$	$\sigma_{\text{Tot}}^{\text{a}}$	$\Delta_{\text{LTE}}^{\text{c}}$
Fe I	84	5.64	0.01	0.05	-1.86	0.05	-0.17
Fe II	20	5.64	0.03	0.11	-1.86	0.11	-0.11
Na I	1	4.13	0.10	0.15	-0.25	0.13	0.14
Mg I	3	5.49	0.03	0.05	-0.25	0.03	0.15
Al I	2	3.19	0.06	0.09	-1.40	0.07	0.10
Si I	1	5.30	0.20	0.23	-0.35	0.21	0.14
Ca I	17	4.30	0.02	0.04	-0.18	0.02	0.17
Sc II	7	0.86	0.02	0.09	-0.43	0.05	0.01
Ti I	6	3.13	0.02	0.05	0.04	0.03	0.16
Ti II	25	3.05	0.02	0.09	-0.04	0.05	0.01
Cr I	7	3.83	0.04	0.08	0.05	0.05	0.16
Cr II	4	3.90	0.04	0.11	0.12	0.05	0.01
Mn I	1	3.12	0.10	0.11	-0.45	0.10	0.17
Co I	1	2.65	0.10	0.11	-0.48	0.11	0.17
Ni I	2	4.18	0.06	0.07	-0.16	0.06	0.14
Zn I	2	2.40	0.06	0.07	-0.30	0.06	0.15
Sr II	1	0.96	0.20	0.32	-0.05	0.24	-0.01
Y II	2	0.05	0.08	0.10	-0.30	0.10	0.01
Zr II	2	0.62	0.07	0.10	-0.10	0.10	0.01
Ba II	3	0.40	0.05	0.16	0.08	0.08	0.02
La II	3	-0.35	0.03	0.08	0.41	0.08	0.01
Ce II	1	0.07	0.05	0.09	0.35	0.08	0.02
Pr II	1	-0.44	0.10	0.12	0.70	0.12	0.02
Nd II	2	0.14	0.09	0.11	0.58	0.11	0.02
Eu II	3	-0.49	0.06	0.12	0.85	0.08	0.01
Gd II	1	-0.04	0.05	0.11	0.70	0.08	0.01
Dy II	1	0.19	0.10	0.12	0.95	0.12	0.01
Th II	1	<-0.79	<1.05

Notes.

^a The total error refers to the combination of random and systematic errors (where the latter are due to uncertainties in the atmospheric parameters), calculated according to Equations (A1), (A4), and (A5) in McWilliam et al. (2013). Errors in $\log \epsilon$ and $[X/\text{Fe}]$ are listed separately.

^b $[\text{Fe}/\text{H}]$ is given for Fe I and Fe II.

^c Δ_{LTE} shows the offsets in $[X/\text{Fe}]$ ratios that occur when the LTE atmospheres are used.

correction of -0.41 dex, which would make the Na abundance significantly subsolar. NLTE corrections to the Al lines may be as large as $+0.6$ to 0.8 dex in this temperature, surface gravity, and metallicity range (Nordlander & Lind 2017).

3.2. α Elements

The α elements with detectable lines in J0937–0626 include Mg, Si, Ca, and Ti; the O lines are too weak. The three Mg I lines at 4167, 4703, and 5528 Å and the Si I line at 3905 Å were synthesized (see Figure 2), while EWs were measured for 17 Ca I lines, six Ti I lines, and 25 Ti II lines. Mashonkina et al. (2016) show that NLTE corrections ~ 0.1 dex may be required for Ca, with larger and smaller corrections for Ti I and Ti II, respectively (though note that the highest temperature they consider is 5000 K). The $[X/\text{Fe}]$ ratios for Mg, Si, and Ca are subsolar, while $[\text{Ti}/\text{Fe}]$ is roughly solar; these ratios are subsolar even when LTE parameters are used. Placco et al. (2018) also found a low $[\alpha/\text{Fe}] = -0.09$ based on a medium-resolution spectrum.

3.3. Iron-peak Elements and Zinc

EWs were measured for seven Sc II, seven Cr I, four Cr II, one Mn I, one Co I, and three Ni I lines. The $[\text{Cr I}/\text{Fe}]$ ratio is

expected to suffer from small NLTE effects; Bergemann & Cescutti (2010) find corrections <0.2 dex. The Mn I and Co I lines also require NLTE corrections on the order of $+0.4$ (Bergemann & Gehren 2008) and $+0.6$ dex (Bergemann et al. 2010), respectively, according the MPlA NLTE correction database³⁰ (though note that none of the models extends to J0937–0626’s surface gravity). None of these NLTE corrections was applied. The Zn I lines at 4722 and 4810 Å were synthesized. The LTE $[\text{Sc}/\text{Fe}]$, $[\text{Mn}/\text{Fe}]$, $[\text{Co}/\text{Fe}]$, and $[\text{Ni}/\text{Fe}]$ ratios are all subsolar, $[\text{Cr}/\text{Fe}]$ is slightly enhanced, and $[\text{Zn}/\text{Fe}]$ is slightly subsolar.

3.4. Neutron-capture Elements

The Sr abundance in J0937–0626 was derived from the relatively strong 4215 Å line, Y was derived from the weak 4883 and 4900 Å lines, and Zr was derived from the 4161 and 4208 Å lines. Unlike the lighter elements, Sr and Zr yield approximately solar $[X/\text{Fe}]$ ratios; Y is slightly subsolar.

Barium and europium are the elements used for classification of r -I and r -II stars. The 5853, 6141, and 6496 Å Ba II lines were used (the 4554 Å line is too strong), while the 3819, 4129, and 4205 Å Eu II lines were used. J0937–0626 has a roughly solar $[\text{Ba}/\text{Fe}] = 0.08 \pm 0.05$ but an enhanced $[\text{Eu}/\text{Fe}] = 0.85 \pm 0.06$, making it an r -I star. Its low $[\text{Ba}/\text{Eu}] = -0.77 \pm 0.07$ indicates that it has received minimal contamination from the main s -process. Lines of Ce II, Pr II, Nd II, Gd II, and Dy II are detectable and also indicate enhancement. Figure 3 shows syntheses of Ba, Pr, and Eu lines. An upper limit is derived from the Th II line at 4019 Å.

4. Discussion

Relative to Fe, J0937–0626 has subsolar $[X/\text{Fe}]$ ratios for nearly all elements (with the exception of Cr and possibly Ti) other than the neutron-capture elements. It has approximately solar $[X/\text{Fe}]$ ratios for Sr, Y, Zr, and Ba, yet is enhanced in La, Ce, Pr, Nd, Eu, Gd, and Dy. Below, J0937–0626’s abundance patterns are compared to other MW halo stars and dwarf galaxy stars (Section 4.1), including the subset of “Fe-enhanced” metal-poor stars. Scenarios to explain the light, α , and Fe-peak elements are explored in Section 4.2. The r -process enhancement and patterns in J0937–0626 are discussed in Section 4.3, while the kinematics are discussed in Section 4.4.

4.1. Comparisons with MW and Dwarf Galaxy Stars

Figure 4 demonstrates that J0937–0626 has low $[\text{Mg}/\text{Fe}]$ and $[\text{Ca}/\text{Fe}]$ relative to MW field stars, along with $[\text{Si}/\text{Fe}]$ and $[\text{Ti}/\text{Fe}]$. J0937–0626 therefore has a deficiency of α elements, relative to Fe, compared to MW field stars. This is a phenomenon usually seen in dwarf galaxy stars (e.g., Shetrone et al. 2003; Tolstoy et al. 2009), where lower $[\alpha/\text{Fe}]$ at a given $[\text{Fe}/\text{H}]$ is usually interpreted as a sign of enrichment from Type Ia supernovae (SNe Ia) which produce lots of Fe, but few α elements (e.g., Lanfranchi et al. 2008).³¹ However, with the exception of the neutron-capture elements (which will be discussed in Section 4.3), most of J0937–0626’s $[X/\text{Fe}]$ ratios are lower than MW field stars at the same metallicity, including Sc and Ni (Figure 5; though note that Mn and Cr agree with

³⁰ <http://nlte.mpia.de>

³¹ Note that J0937–0626 is more iron- and α -poor than the low- α disk stars (e.g., Helmi et al. 2018), as will be discussed in Section 4.4.

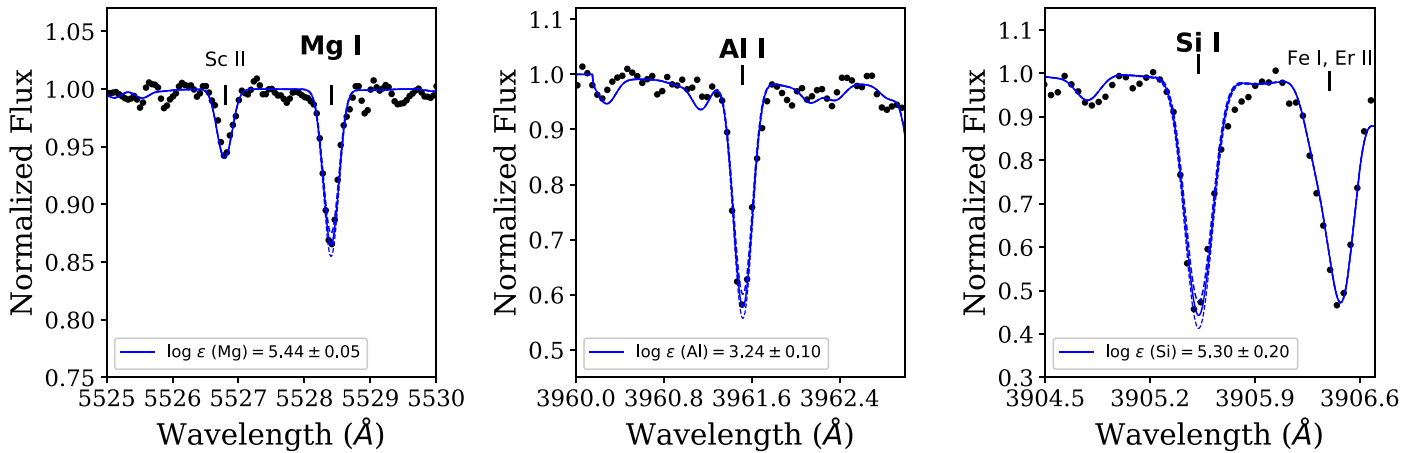


Figure 2. Syntheses of Mg, Al, and Si lines. The solid line shows the best fit, while the dashed lines show the 1σ uncertainties.

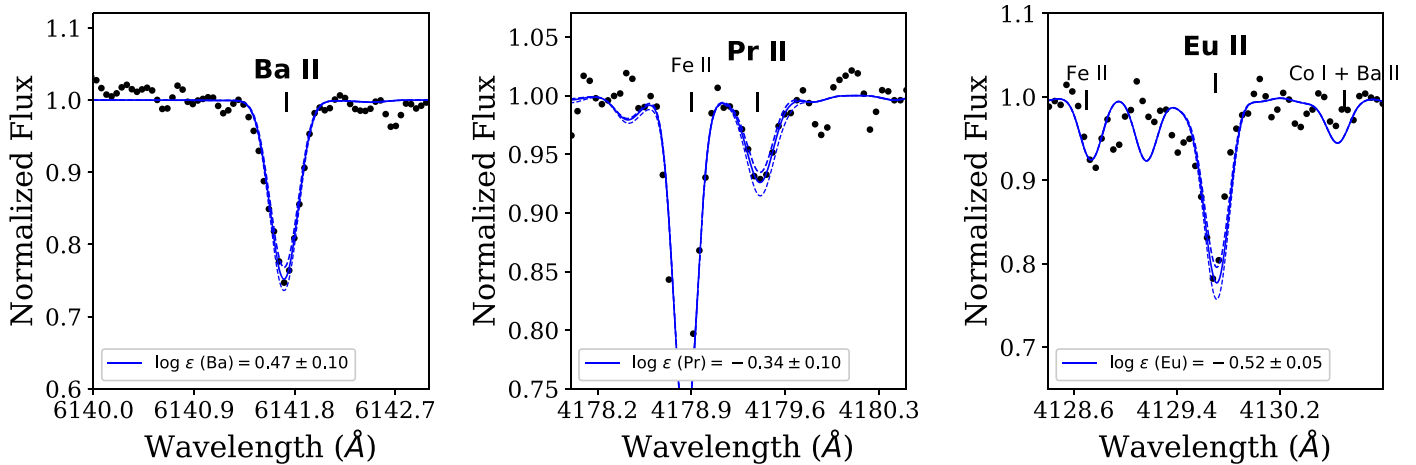


Figure 3. Syntheses of Ba, Pr, and Eu lines.

MW stars). In this respect, J0937–0626 resembles the class of MW and dwarf galaxy stars that have been called “Fe-enhanced” metal-poor stars (Yong et al. 2013), those that show subsolar $[X/Fe]$ ratios in nearly every element.³² Also shown in Figures 4 and 5 are a selection of low- α or “Fe-enhanced” metal-poor stars from the MW halo, HE 1207–3108 (Yong et al. 2013), HE 0533–5340 (Cohen et al. 2013), SDSS J001820.5-093939.2 (Aoki et al. 2014), and BD+80° 245 (Carney et al. 1997; Ivans et al. 2003; Roederer et al. 2014b), along with low- α stars from four dwarf galaxies, Ursa Minor (UMi COS 171; Cohen & Huang 2010), Carina (Car 612; Venn et al. 2012), Horologium I (Hor I, three stars; Nagasawa et al. 2018), and Ret II (DES J033548–540349, hereafter DES J0335–5403; Ji et al. 2016). These comparison stars indeed show the characteristic subsolar $[X/Fe]$ ratios found in J0937–0626, albeit with slightly different values. J0937–0626 can therefore be considered to be another one of these “Fe-enhanced” metal-poor stars.

A more detailed element-by-element comparison is shown in Figure 6, which plots $[X/Fe]$ ratios for each element. Following

Yong et al. (2013), only stars with similar metallicities are shown—here, J0937–0626 ($[Fe/H] = -1.86$) is shown along with DES J0335–5403 ($[Fe/H] = -2.19$; Ji et al. 2016) and BD +80° 245 ($[Fe/H] = -2.04$; Ivans et al. 2003; Roederer et al. 2014b). For the elements through Zn, J0937–0626’s abundance ratios are similar to BD+80° 245. DES J0335–5403 shows a similar abundance pattern, with the exception of Ca, Ti, Co, and Zn, which all have higher $[X/Fe]$ ratios than J0937–0626.

To investigate the source of J0937–0626’s unusual abundance ratios, the procedure from McWilliam et al. (2018), who performed a re-analysis of UMi COS 171, is followed. First, note that the removal of ~ 0.6 dex of Fe from J0937–0626 would shift its $[\alpha/Fe]$ ratios to normal values—this shift would lead to a lower metallicity of $[Fe/H] = -2.50$. The specific yields from the event(s) that created J0937–0626’s unusual abundance pattern can then be investigated through a comparison with a star at $[Fe/H] = -2.50$ that formed in the same environment. McWilliam et al. (2018) used a more metal-poor star in UMi; however, such a star cannot be confidently identified for J0937–0626. Instead, the average abundance pattern of MW stars with $-2.6 \leq [Fe/H] \leq -2.4$ is utilized. To make this comparison as homogeneous as possible, the average abundances of the MW stars in this metallicity range from

³² The low Sc in J0937–0626 is also somewhat reminiscent of the metal-poor bulge stars observed by Casey & Schlafman (2015), though those stars have otherwise normal $[X/Fe]$ ratios.

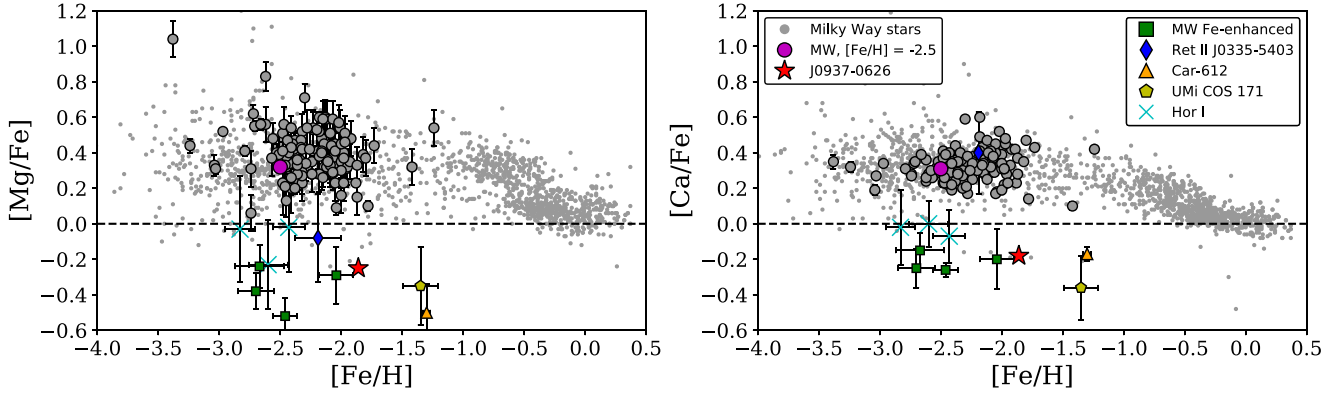


Figure 4. $[Mg/Fe]$ and $[Ca/Fe]$ ratios as a function of $[Fe/H]$. J0937–0626’s abundances and uncertainties are shown as red stars. The MW stars are shown as gray points (Venn et al. 2004; Reddy et al. 2006); the stars from Sakari et al. (2018a) are the larger outlined circles. The MW Fe-enhanced stars from Yong et al. (2013), Cohen et al. (2013), and Roederer et al. (2014b) are shown with green squares. Stars from four dwarf galaxies are shown: Ret II DES J0335–5403, with blue diamonds (Ji et al. 2016); UMi COS 171, with a yellow pentagon (Cohen & Huang 2010); Car-612, with an orange triangle (Venn et al. 2012); and three stars from Hor I, with cyan crosses (Nagasawa et al. 2018). The magenta circle shows the average of the Sakari et al. (2018a) stars with $-2.6 \leq [Fe/H] \leq -2.4$.

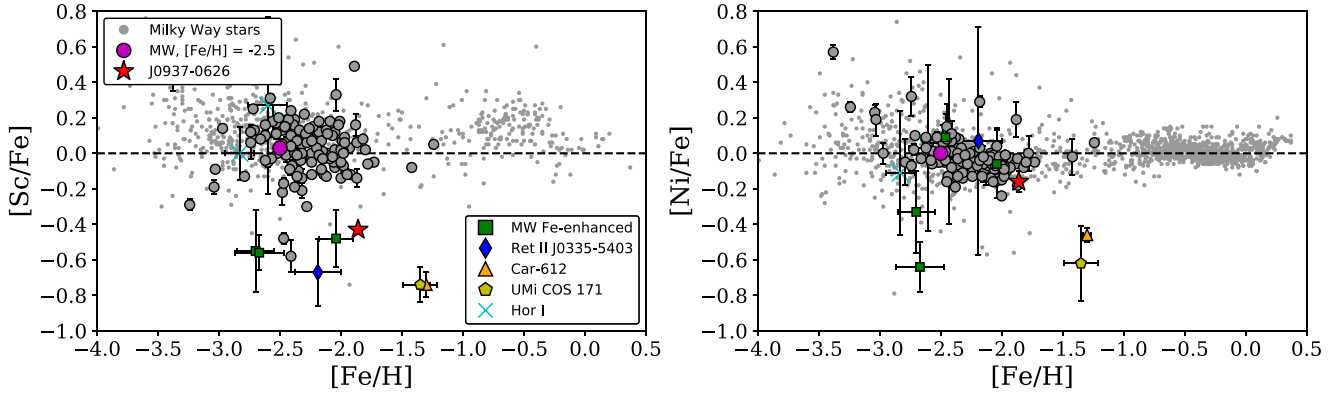


Figure 5. $[Sc/Fe]$ and $[Ni/Fe]$ ratios as a function of $[Fe/H]$. Points are as in Figure 4.

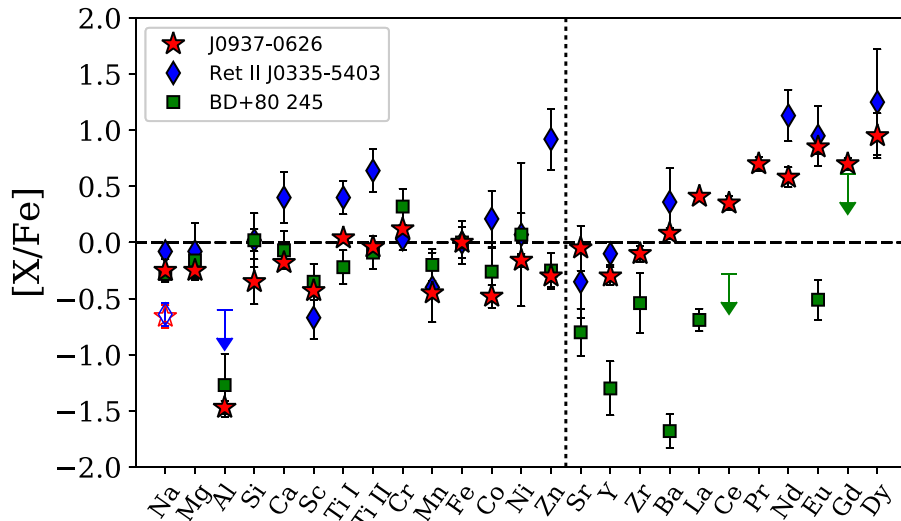


Figure 6. $[X/Fe]$ ratios for each element in J0937–0626 (red stars), DES J0335–5403 (blue diamonds; Ji et al. 2016), and BD+80° 245 (green squares; Ivans et al. 2003 for Na, Si, La, and Eu; Roederer et al. 2014b for all other elements). NLTE-corrected Na abundances for J0937–0626 and DES J0335–5403 are shown with open symbols; NLTE-corrected values are not shown for Mn and Co. The neutron-capture elements are on the right, separated by a dotted line.

Sakari et al. (2018a) are used. These stars have been analyzed with the same techniques as for J0937–0626, using the same $\langle 3D \rangle$ NLTE corrections to Fe I lines, the same model

atmospheres, and the same line lists. (However, note that none of the stars in Sakari et al. 2018a is as hot as J0937–0626.) These average values are also shown in Figures 4 and 5. Note

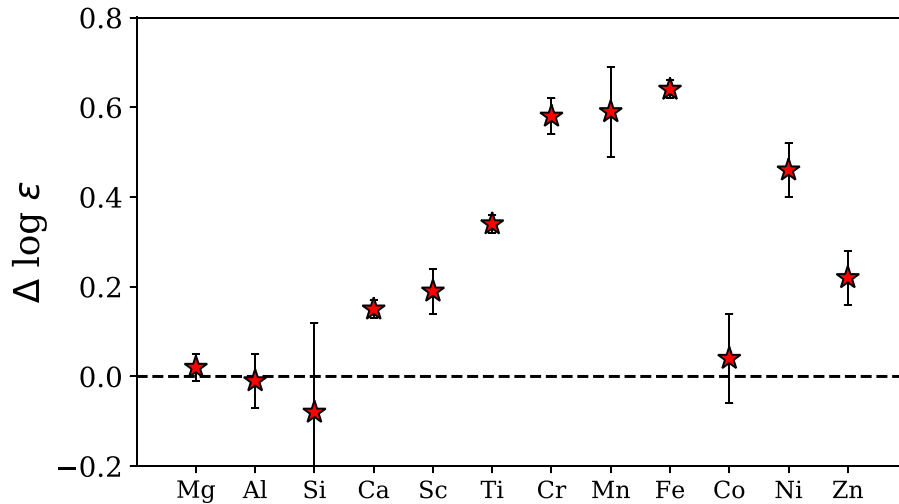


Figure 7. Differences in $\log \epsilon$ abundance between J0937–0626 and a typical MW star at $[\text{Fe}/\text{H}] = -2.5$ (the Fe abundance that J0937–0626 would need to have normal $[\alpha/\text{Fe}]$ ratios). Ti II and Cr II are chosen to represent Ti and Cr, to minimize NLTE effects. Note that LTE abundances are shown, though both Mn and Co require NLTE corrections; however, these corrections differ by $\lesssim -0.1$ between stars at $[\text{Fe}/\text{H}] = -1.86$ and $[\text{Fe}/\text{H}] = -2.5$, according to the MPA NLTE database.

that the NLTE corrections to the Mn and Co abundances will differ slightly between $[\text{Fe}/\text{H}] = -1.86$ and $[\text{Fe}/\text{H}] = -2.5$; however, the MPA NLTE correction database indicates that the corrections are $\lesssim 0.1$ dex higher at $[\text{Fe}/\text{H}] = -2.5$ for both Mn and Co (Bergemann & Gehren 2008; Bergemann et al. 2010).

Figure 7 then shows the differences in the $\log \epsilon$ abundance between J0937–0626 and the average MW values at $[\text{Fe}/\text{H}] = -2.5$. This comparison indicates that one or more nucleosynthetic events have significantly enriched J0937–0626 in Cr, Mn, Fe, and Ni, with minor enhancement in Ca, Sc, Ti, and Zn.

4.2. Potential Explanations for Light, α , and Fe-peak Abundances

J0937–0626 therefore either shows an enhancement in some Fe-peak elements relative to the light and α elements, or a relative deficiency in the light and α elements. Three possible scenarios to explain this abundance pattern are considered. First, the abundances could reflect an evolutionary effect, such as radiative levitation. Second, the entire abundance pattern could be representative of enrichment from a single object. Finally, the abundance profile could be due to multiple progenitors, as a consequence of extended star formation. These possibilities are addressed below.

Radiative levitation in hot horizontal branch stars has been shown to enhance Fe-peak abundances by large amounts (up to 3 dex; Behr 2003). Reproducing the observed $[\text{X}/\text{Fe}]$ ratios would require levitation only for the Fe-peak (and neutron-capture) elements. Furthermore, significant abundance differences have only been observed in the hottest horizontal branch stars, with temperatures above $\sim 11,000$ K (Lovisi et al. 2012; Tailo et al. 2017); at 5875 K, J0937–0626 is not expected to experience significant radiative levitation. Such effects are also not seen in other field horizontal branch stars (e.g., HD 222925; Roederer et al. 2018b). This scenario therefore seems unlikely to explain the abundance pattern in J0937–0626.

Enrichment by a single source has also been invoked as an explanation for α -poor, very metal-poor stars. Standard core-collapse supernovae are unlikely to produce sufficiently low $[\alpha/\text{Fe}]$ ratios to match those in J0937–0626; however, more

exotic supernovae can create unusual abundance signatures. Aoki et al. (2014) found that a pair-instability supernova (PISN) could explain the abundance signature of SDSS J0018–0939, a star at $[\text{Fe}/\text{H}] \sim -2.5$. They based this conclusion on the star’s low $[\alpha/\text{Fe}]$ (with the exception of Si), $[\text{C}/\text{Fe}]$, and $[\text{Co}/\text{Fe}]$ ratios, as well as its strong odd–even effect (contrasting abundances in odd versus even elements), though they do note that the predicted odd–even effect is stronger than observed. Nagasawa et al. (2018) also explore the possibility that a PISN enriched their three stars in Hor I (with metallicities ranging from $[\text{Fe}/\text{H}] = -2.8$ to -2.5), finding that none of the PISN models can perfectly reproduce the abundance pattern. They note that the models do not match the observed Fe-peak abundances (particularly their solar $[\text{Co}/\text{Fe}]$ ratios) and predict a strong odd–even effect that is not observed. J0937–0626 also has low $[\alpha/\text{Fe}]$ and $[\text{Co}/\text{Fe}]$; however, the Heger & Woosley (2002, 2010) PISN models do not match all the abundance ratios. In particular, a PISN cannot produce enough Sc or Zn, and produces a stronger odd–even effect than observed. It therefore seems unlikely that J0937–0626 was enriched by a single PISN.

Nishimura et al. (2017) and Tsujimoto & Nishimura (2018) have noted that neutrino heating in magnetorotational supernovae may be a viable site for Zn production (along with Fe, Co, and Ni) in metal-poor environments. Using samples of stars in the MW, Tsujimoto & Nishimura (2018) argue that a high $[\text{Zn}/\text{Mg}]$ ratio at very low metallicity indicates a high frequency of magnetorotational supernovae; at higher metallicities, a high $[\text{Zn}/\text{Mg}]$ may also reflect the onset of SNe Ia (see their Figure 3). Given its high $[\text{Zn}/\text{Mg}] = -0.05$ (compared to an average $[\text{Zn}/\text{Mg}] = -0.40$ at $[\text{Fe}/\text{H}] = -1.9$), it is tempting to speculate that J0937–0626 may have been enriched by a magnetorotational supernova; however, by $[\text{Fe}/\text{H}] = -2.5$, the contributions from magnetorotational supernovae are already expected to be decreasing. Instead, Tsujimoto & Nishimura (2018) argue that the Zn enhancement in DES J0335–5403 and a star in the Draco dwarf galaxy is due to SNe Ia. Detailed yields from magnetorotational supernovae are necessary to fully address this possibility.

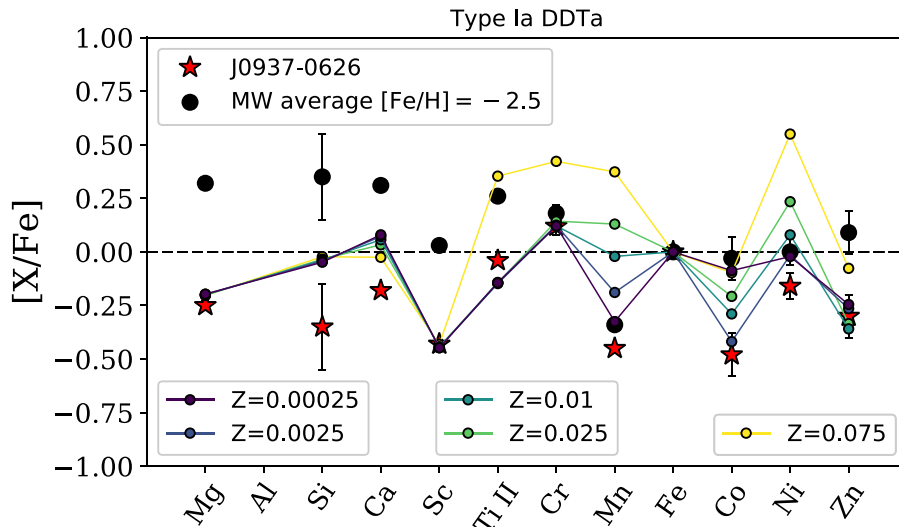


Figure 8. Comparisons of “DDTa” Ia yields from Badenes et al. (2003, 2008, as reported by McWilliam et al. 2018) with the J0937–0626 abundances (red stars). The Ia yields are added to the average MW abundances at $[\text{Fe}/\text{H}] \sim -2.5$ (black circles) so that the $[\text{Fe}/\text{H}]$ is increased to J0937–0626’s value. The five lines show the Ia yields for five different metallicities. Note that the yield patterns change when the physics of the explosion are altered; the “DDTa” model represents the best fit to J0937–0626’s abundances.

Kobayashi et al. (2014) have also argued that low $[\alpha/\text{Fe}]$ in extremely metal-poor stars can be the nucleosynthetic result of $\sim 10\text{--}20 M_{\odot}$ core-collapse supernovae or hypernovae. They suggest that hypernovae would produce a high $[\text{Zn}/\text{Fe}] > 0.3$, which is not observed in J0937–0626. The abundance pattern for $\sim 10\text{--}20 M_{\odot}$ supernovae also does not quite match the pattern in J0937–0626, particularly the high α and Zn and the pattern of Fe-peak elements. Core-collapse supernovae on their own are therefore not a likely source of the abundance patterns in J0937–0626. It is also worth noting that J0937–0626 is more metal-rich than the other targets whose abundances were explained by a single progenitor.

A more likely explanation for the abundance patterns in Figures 6 and 7 is that J0937–0626’s host environment experienced extended star formation and chemical enrichment, with core-collapse supernovae building the metallicity up to $[\text{Fe}/\text{H}] = -2.5$ before a second event produced a significant amount of Cr, Mn, Fe, and Ni and a smaller amount of Ca, Sc, Ti, and Zn. The most likely option is enrichment from a type Ia supernova, which are known to produce Fe-peak elements (e.g., Iwamoto et al. 1999; Badenes et al. 2003, 2008). The precise yields depend on parameters such as white dwarf mass, metallicity, and the physics of the explosion.

Figures 8 and 9 show comparisons between J0937–0626’s $[\text{X}/\text{Fe}]$ abundance ratios and Ia yields, added to the background MW average at $[\text{Fe}/\text{H}] \sim -2.5$. The Chandrasekhar-mass “DDTa” model from Badenes et al. (2003, 2008) is shown in Figure 8, using the yields from McWilliam et al. (2018), for five different metallicities. (Note that the other models overpredict $[\text{Mn}/\text{Fe}]$.) Though the agreement for $Z = 0.0025$ is generally decent, none of these metallicities can perfectly reproduce the pattern in the Fe-peak elements. At all metallicities, this Ia model also overproduces Si and Ca and (except for the highest-metallicity model) underproduces Ti. Figure 9 then shows sub-Chandrasekhar mass models from E. Bravo, with the yields from McWilliam et al. (2018), for two white dwarf masses: $1.06 M_{\odot}$ and $1.15 M_{\odot}$. For UMi COS 171, McWilliam et al. (2018) found that a sub-Chandrasekhar mass model provided a better fit to the

abundances, particularly the low $[\text{Mn}/\text{Fe}]$ and $[\text{Ni}/\text{Fe}]$. Indeed, there is decent agreement with Mn and Co in J0937–0626 for both sub-Chandrasekhar masses. As with the Ia case, both sub-Chandrasekhar models overpredict the amount of Si and Ca.

Though no model perfectly matches the pattern in J0937–0626, its abundances are generally consistent with enrichment from an SN Ia, possibly one with a sub-Chandrasekhar mass. However, the precise Ia yields depend on the physical conditions of the models (e.g., explosion energy). Similarly, if the background composition of J0937–0626’s birth environment was different from the MW composition (e.g., if the Si and Ca abundances were lower at $[\text{Fe}/\text{H}] = -2.5$), then these predicted yields would also change. The general enhancement in Fe-peak elements supposes enrichment from an SN Ia.

It is worth noting that none of the proposed scenarios for enrichment in Fe-peak elements is likely to have created a significant number of neutron-capture elements. Neither SNe Ia nor PISNe will create r -process elements (e.g., Heger & Woosley 2002), while standard core-collapse supernovae have been ruled out as a significant source of r -process elements (e.g., Arcones & Thielemann 2013). Though magnetorotational supernovae have been identified as possible sources of both Fe-peak and r -process elements, Nishimura et al. (2017) showed that the supernovae that produce significant amounts of Fe, Ni, and Zn do not produce much Eu, and vice versa. The enhancement of neutron-capture elements therefore likely requires enrichment by a separate event.

4.3. r -process Enhancement and Patterns

Unlike many of the light, α , and Fe-peak elements, J0937–0626 shows solar or supersolar $[\text{X}/\text{Fe}]$ ratios for the neutron-capture elements. At $[\text{Eu}/\text{Fe}] = 0.85 \pm 0.06$, J0937–0626 is an r -I star; its low $[\text{Ba}/\text{Eu}] = -0.77 \pm 0.07$ implies that its Eu enhancement is due to the r -process. Note that red horizontal branch stars have been discovered to be r -process enhanced (Roederer et al. 2014a), including HD 222925 (Roederer et al. 2018b), so this is not a unique feature of J0937–0626. Sr, Y, and Zr are also roughly solar, while La, Ce, Pr, Nd, Gd, and Dy are enhanced. Figure 10 shows that J0937–0626’s

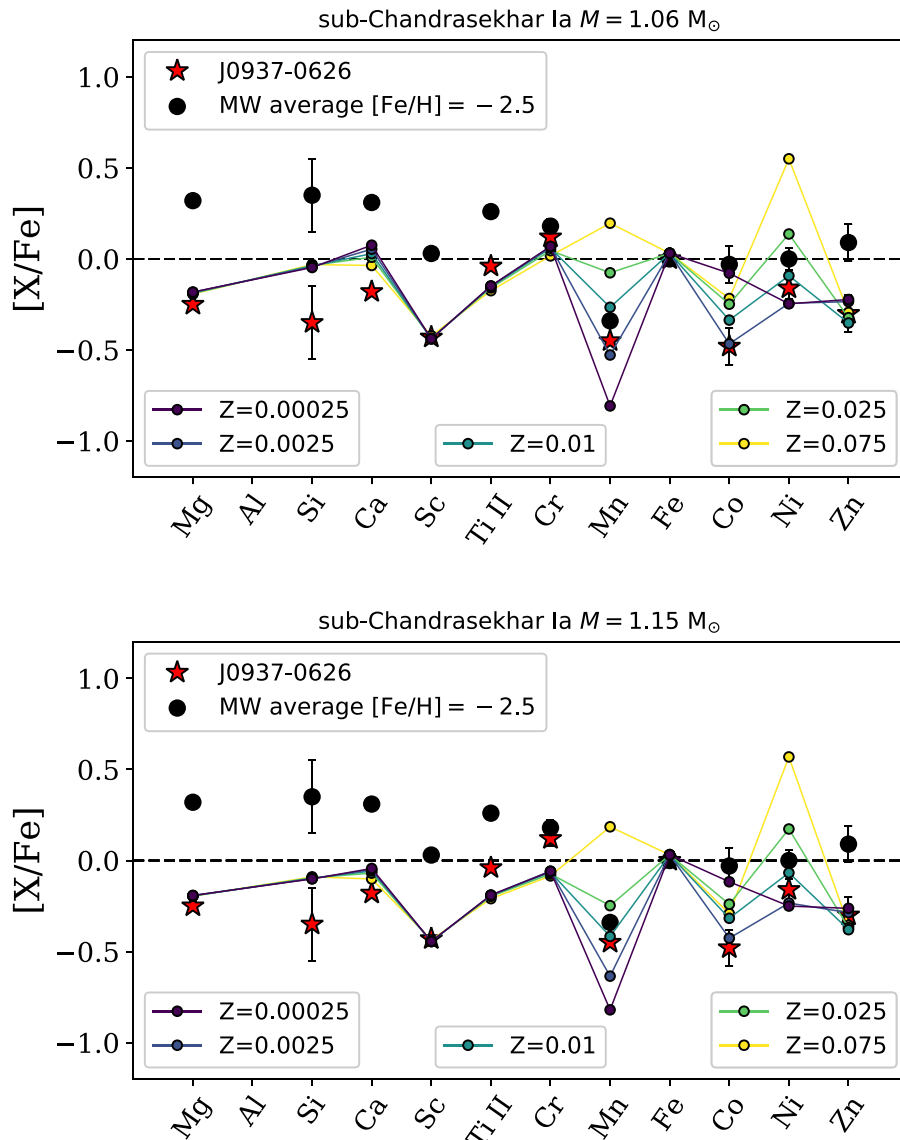


Figure 9. Comparisons of sub-Chandrasekhar mass Ia yields from E. Bravo, as reported by McWilliam et al. (2018) with J0937–0626 abundances. Points are as in Figure 8.

neutron-capture abundance pattern is generally consistent with the r -process residual in the Sun and two stars in Reticulum II (though, like Ret II, Sr, Y, and Zr in J0937–0626 are slightly lower than the solar residual, as discussed in Ji et al. 2016). The pattern is inconsistent with the solar s -process. The low [Sr/Ba] also indicates that significant contributions from the weak s -process in rapidly rotating massive stars (e.g., Chiappini et al. 2011; Frischknecht et al. 2012; Cescutti et al. 2013; Frischknecht et al. 2016) are unlikely. The upper limit in Th also implies $\log \epsilon(\text{Th}/\text{Eu}) < -0.3$.

Figure 11 shows J0937–0626’s slightly enhanced [Ba/Fe] and strongly enhanced [Eu/Fe], relative to the “normal” and “Fe-enhanced” MW field stars. The r -process enhancement in J0937–0626 makes it unlike most of the other “Fe-enhanced” metal-poor stars, whose low [X/Fe] ratios persist through the neutron-capture elements (including BD+80° 245; see Figure 6).³³ Instead, the r -process enhancement in J0937–0626

more closely resembles DES J0335–5403, the Ret II star, which is also an r -I star.

Section 4.1 demonstrated that many of the [X/Fe] ratios could be brought into agreement with MW stars by removing 0.6 dex of Fe. This would increase the [X/Fe] ratios of the r -process elements, as shown by the maroon star in Figure 11. If the r -process event occurred prior to the Fe-peak event, then J0937–0626 would have been an r -II star if the Fe-peak event had not occurred. Furthermore, if J0937–0626 originated in a dwarf galaxy (see Section 4.4), this dwarf galaxy would likely have contained a population of highly r -process-enhanced stars, similar to Ret II. Indeed, though none has been linked to J0937–0626, many of the r -II stars in the MW have been kinematically identified as probable captures from dwarf galaxies (Roederer et al. 2018a; Sakari et al. 2018a, 2018b), hinting that many r -II stars have originated in r -process-enhanced dwarf galaxies like Ret II.

4.4. Kinematics

Figure 12 shows a Toomre diagram of MW field stars from *Gaia* DR2 (using the halo stars within 1 kpc from

³³ Note that, though there are r -process-enhanced stars in UMi, COS 171 is not r -process enhanced.

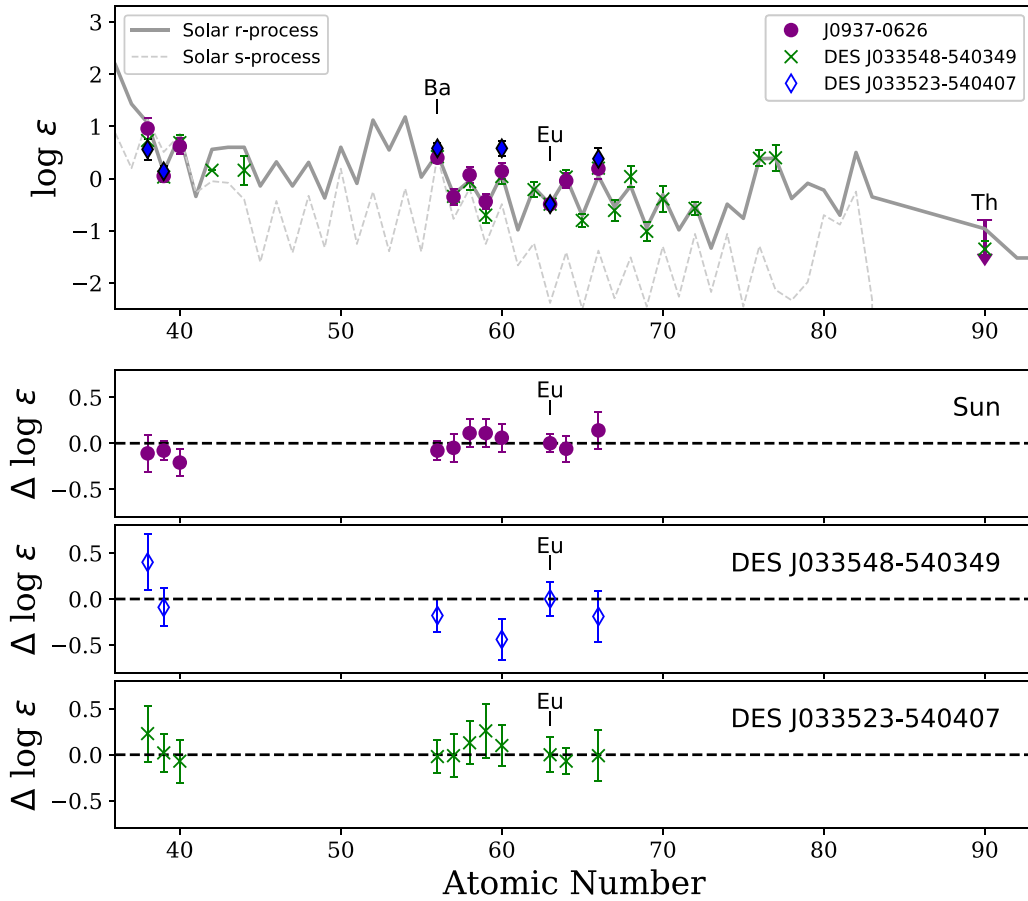


Figure 10. Top: abundances of neutron-capture elements in J0937–0626 along with the total errors (Table 3); also shown are the r - and s -process patterns in the Sun (gray line; Arlandini et al. 1999) and two stars in Ret II (Ji et al. 2016). The solar r -process pattern and the Ret II abundances are shifted to the Eu abundance in J0937–0626; the solar s -process pattern is shifted to match the Ba abundance. Bottom three panels: the residuals between J0937–0626 and the Sun, DES J033548–540349, and DES J033523–540407.

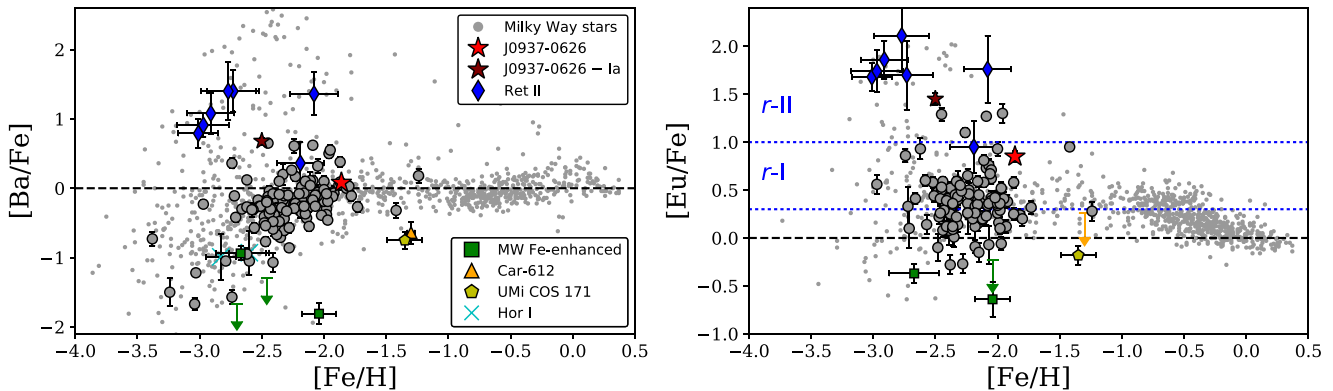


Figure 11. $[\text{Ba}/\text{Fe}]$ and $[\text{Eu}/\text{Fe}]$ as a function of $[\text{Fe}/\text{H}]$. The points are as in Figure 4, except that the MW average is not shown. Instead, the maroon star shows how J0937–0626’s abundance ratios would change with the removal of 0.6 dex of Fe. The right panel also shows the r -I and r -II $[\text{Eu}/\text{Fe}]$ definitions.

Koppelman et al. 2018), along with distinctions between prograde and retrograde orbits. Its velocities (derived with the `gal_uv` code³⁴) show that J0937–0626 resides in the MW halo, with a retrograde orbit. Previous work has found that a significant number of MW r -I and r -II stars have retrograde orbits (Roederer et al. 2018a; Sakari et al. 2018a, 2018b) and may have been accreted from satellite galaxies. J0937–0626’s

kinematics also suggest that it may also have been accreted from a satellite galaxy.

Koppelman et al. (2018) and Roederer et al. (2018a) have also identified specific groups of stars with similar kinematics which may have originated in the same galaxy. Recently, Helmi et al. (2018) argued that the majority of the retrograde stars from Koppelman et al.’s analysis are due to a single merger event from a galaxy with a mass slightly higher than the Small Magellanic Cloud, which they named Gaia-Enceladus. They also found that the Gaia-Enceladus stars have slightly

³⁴ https://github.com/segasai/astrolibpy/blob/master/astrolib/gal_uv.py

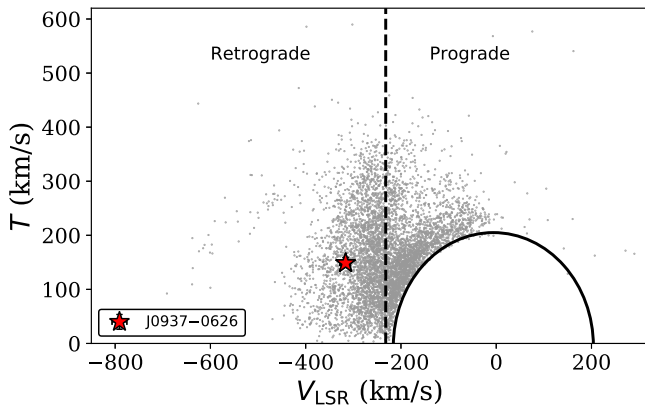


Figure 12. Toomre diagram, where $T = \sqrt{U^2 + W^2}$, utilizing parallaxes and proper motions from *Gaia* DR2. J0937–0626 is shown as a red star. The gray points are MW halo stars within 1 kpc, from Koppelman et al. (2018); the large black circle shows their definition for halo membership, where disk stars lie within the circle.

lower $[\alpha/\text{Fe}]$ ratios than MW stars (also see Nissen & Schuster 2010 and Hayes et al. 2018). J0937–0626 lies approximately in the correct kinematic space for Gaia-Enceladus stars; however, its $[\text{Fe}/\text{H}]$ and $[\alpha/\text{Fe}]$ ratios are lower than the majority of the Gaia-Enceladus stars. It is still possible that J0937–0626 was brought in by the same merger event if it experienced inhomogeneous mixing within the larger galaxy (similar to the scenario proposed by Venn et al. 2012 for Carina). Full orbital calculations will also be essential for identifying J0937–0626’s birth site and locating other stars from the same environment.

Roederer et al. (2018a) examined the kinematics of 35 *r*-II stars with high-quality *Gaia* data, and identified several groups with similar orbits and metallicities. This technique could be used to identify other stars from the same birth environment as J0937–0626: its chemistry and kinematics should be similar to other *r*-I stars from the same birth environment; similarly, if that environment was enriched in *r*-process elements before the event that created the Fe-peak enrichment, J0937–0626 should have similar kinematics as more metal-poor *r*-II stars. RPA discoveries of more *r*-I and *r*-II stars, combined with future *Gaia* data, will identify other stars that could have originated in the same environment as J0937–0626.

5. Conclusions

RAVE J093730.5–062655 is a moderately *r*-process-enhanced ($[\text{Eu}/\text{Fe}] = +0.85 \pm 0.1$), metal-poor ($[\text{Fe}/\text{H}] = -1.86$) horizontal branch star on a retrograde orbit in the MW halo that was identified by the RPA. Most of its $[\text{X}/\text{Fe}]$ abundance ratios are distinct from those of typical MW field stars, particularly its subsolar $[\alpha/\text{Fe}]$ (e.g., $[\text{Mg}/\text{Fe}] = -0.25 \pm 0.04$, $[\text{Ca}/\text{Fe}] = -0.18 \pm 0.03$), light element ($[\text{Na}/\text{Fe}] = -0.25 \pm 0.13$), and some Fe-peak ratios (e.g., $[\text{Ni}/\text{Fe}] = -0.18 \pm 0.06$). J0937–0626 seems to have the abundance pattern typical of a “normal” MW star at $[\text{Fe}/\text{H}] \sim -2.5$ that was diluted by ejecta from an event that created ~ 0.6 dex of Fe-peak elements. Although none of the models perfectly fits the abundance patterns in J0937–0626, the best candidate for this Fe-peak enrichment is an SN Ia.

J0937–0626’s *r*-process enrichment is unlikely to have been caused by an SN Ia. Instead, its birth environment may have been enhanced in *r*-process elements prior to the enrichment from the SN Ia; J0937–0626 therefore could have been an *r*-II

star were it not for the occurrence of the SN Ia. In this sense, J0937–0626 may be similar to the metal-rich *r*-I star in Reticulum II. Ultimately, J0937–0626’s chemical abundances and kinematics indicate that it was likely accreted from a satellite dwarf galaxy. J0937–0626’s host galaxy may have been responsible for depositing other stars into the MW halo, possibly even more metal-poor *r*-II stars. Additional discoveries of *r*-I and *r*-II stars by the RPA, combined with proper motions and parallaxes from *Gaia*, will enable specific subgroups to be identified in the future.














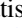

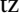
The authors thank the current and previous observing specialists on the 3.5 m telescope at Apache Point Observatory for their continued help and support. The authors thank the anonymous referee for helpful comments which improved this manuscript. The authors also thank Anish Amarsi and Karin Lind for providing the NLTE grids and assisting with their usage, and Helmer Koppelman for providing the 1 kpc *Gaia* sample.

C.M.S. and G.W. acknowledge funding from the Kenilworth Fund of the New York Community Trust. V.M.P., T.C.B., R.E., A.F., and I.U.R. acknowledge partial support from grant PHY 14-30152 (Physics Frontier Center/JINA/CEE), awarded by the US National Science Foundation. I.U.R. acknowledges additional support from NSF grants AST 16-13536 and AST 18-15403. B.K.G. acknowledges the support of STFC, through the University of Hull’s Consolidated Grant ST/R000840/1. E.K.G. gratefully acknowledges support via Sonderforschungsbereich SFB 881 “The Milky Way System” (subproject A5) of the German Research Foundation (DFG). Funding for RAVE has been provided by: the Leibniz-Institut für Astrophysik Potsdam (AIP); the Australian Astronomical Observatory; the Australian National University; the Australian Research Council; the French National Research Agency; the German Research Foundation (SPP 1177 and SFB 881); the European Research Council (ERC-StG 240271 Galactica); the Istituto Nazionale di Astrofisica at Padova; The Johns Hopkins University; the National Science Foundation of the USA (AST-0908326); the W. M. Keck foundation; the Macquarie University; the Netherlands Research School for Astronomy; the Natural Sciences and Engineering Research Council of Canada; the Slovenian Research Agency; the Swiss National Science Foundation; the Science & Technology Facilities Council of the UK; Opticon; Strasbourg Observatory; and the Universities of Groningen, Heidelberg and Sydney. The RAVE website is at <https://www.rave-survey.org>.

This research is based on observations obtained with the Apache Point Observatory 3.5 m telescope, which is owned and operated by the Astrophysical Research Consortium. This research has made use of the SIMBAD database, operated at CDS, Strasbourg, France. This work has also made use of data from the European Space Agency (ESA) mission *Gaia* (<http://www.cosmos.esa.int/gaia>), processed by the *Gaia* Data Processing and Analysis Consortium (DPAC, <http://www.cosmos.esa.int/web/gaia/dpac/consortium>). Funding for the DPAC has been provided by national institutions, in particular the institutions participating in the *Gaia* Multilateral Agreement.

Software: IRAF (Tody 1986, Tody 1993), DAOSPEC (Stetson & Pancino 2008), MOOG (v2017; Sneden 1973), linemake (<https://github.com/vmplacco/linemake>), gal_uv (https://github.com/segasai/astrolibpy/blob/master/astrolib/gal_uv.py).

ORCID iDs

Charli M. Sakari  <https://orcid.org/0000-0002-5095-4000>
 Ian U. Roederer  <https://orcid.org/0000-0001-5107-8930>
 Vinicius M. Placco  <https://orcid.org/0000-0003-4479-1265>
 Timothy C. Beers  <https://orcid.org/0000-0003-4573-6233>
 Rana Ezzeddine  <https://orcid.org/0000-0002-8504-8470>
 Anna Frebel  <https://orcid.org/0000-0002-2139-7145>
 Terese Hansen  <https://orcid.org/0000-0001-6154-8983>
 Christopher Sneden  <https://orcid.org/0000-0002-3456-5929>
 Kim A. Venn  <https://orcid.org/0000-0003-4134-2042>
 Joss Bland-Hawthorn  <https://orcid.org/0000-0001-7516-4016>
 Kenneth C. Freeman  <https://orcid.org/0000-0001-6280-1207>
 Brad K. Gibson  <https://orcid.org/0000-0003-4446-3130>
 Amina Helmi  <https://orcid.org/0000-0003-3937-7641>
 Georges Kordopatis  <https://orcid.org/0000-0002-9035-3920>
 Andrea Kunder  <https://orcid.org/0000-0002-2808-1370>
 Matthias Steinmetz  <https://orcid.org/0000-0001-6516-7459>

References

- Abbott, B. P., Abbott, R., Abbott, T. D., et al. 2017, *PhRvL*, 119, 1101
 Amarsi, A. M., Lind, K., Asplund, M., Barklem, P. S., & Collet, R. 2016, *MNRAS*, 463, 1518
 Aoki, W., Tominaga, N., Beers, T. C., Honda, S., & Lee, Y. S. 2014, *Sci*, 345, 912
 Arcones, A., & Thielemann, F.-K. 2013, *JPhG*, 40, 3201
 Arlandini, C., Käppeler, F., Wisshak, K., et al. 1999, *ApJ*, 525, 886
 Asplund, M., Grevesse, N., Sauval, J. A., & Scott, P. 2009, *ARA&A*, 47, 481
 Badenes, C., Bravo, E., Borkowski, K. J., & Domínguez, I. 2003, *ApJ*, 593, 358
 Badenes, C., Hughes, J. P., Cassam-Chenaï, G., & Bravo, E. 2008, *ApJ*, 680, 1149
 Bailer-Jones, C. A. L., Rybizki, J., Fouesneau, M., Mantelet, G., & Andrae, R. 2018, *AJ*, 156, 158
 Beers, T. C., & Christlieb, N. 2005, *ARA&A*, 43, 531
 Beers, T. C., Flynn, C., Rossi, S., et al. 2007, *ApJS*, 168, 128
 Behr, B. B. 2003, *ApJS*, 149, 67
 Beniamini, P., Dvorkin, I., & Silk, J. 2018, *MNRAS*, 478, 1994
 Bergemann, M., & Cescutti, G. 2010, *A&A*, 522, 9
 Bergemann, M., & Gehren, T. 2008, *A&A*, 492, 823
 Bergemann, M., Pickering, J. C., & Gehren, T. 2010, *MNRAS*, 401, 1334
 Bland-Hawthorn, J., Sutherland, R., & Webster, D. 2015, *ApJ*, 807, 154
 Brook, C. B., Kawata, D., Scannapieco, E., Martel, H., & Gibson, B. K. 2007, *ApJ*, 661, 10
 Brook, C. B., Stinson, G. S., Gibson, B. K., et al. 2012, *MNRAS*, 426, 690
 Cain, M., Frebel, A., Gull, M., et al. 2018, *ApJ*, 864, 43
 Carney, B. W., Wright, J. S., Sneden, C., Laird, J. B., Aguilar, L. A., & Latham, D. W. 1997, *AJ*, 114, 363
 Casagrande, L., Ramírez, I., Meléndez, J., Bessell, M., & Asplund, M. 2010, *A&A*, 512, 54
 Casey, A. R., & Schlafman, K. C. 2015, *ApJ*, 809, 110
 Cescutti, G., Chiappini, C., Hirschi, R., Meynet, G., & Frischknecht, U. 2013, *A&A*, 553, 51
 Cescutti, G., Romano, D., Matteucci, F., Chiappini, C., & Hirschi, R. 2015, *A&A*, 577, A139
 Chiappini, C., Frischknecht, U., Meynet, G., et al. 2011, *Natur*, 472, 454
 Chornock, R., Berger, E., Kasen, D., et al. 2017, *ApJL*, 848, L19
 Cohen, J. G., Christlieb, N., Thompson, I., et al. 2013, *ApJ*, 778, 56
 Cohen, J. G., & Huang, W. 2010, *ApJ*, 719, 931
 Côté, B., Eichler, M., Arcones, A., et al. 2018, arXiv:1809.03525
 Drout, M. R., Piro, A. L., Shappee, B. J., et al. 2017, *Sci*, 358, 1570
 El-Badry, K., Bland-Hawthorn, J., Wetzel, A., et al. 2018, *MNRAS*, 480, 652
 Ezzeddine, R., Frebel, A., & Plez, B. 2017, *ApJ*, 847, 142
 Ezzeddine, R., Merle, T., & Plez, B. 2016, *AN*, 337, 850
 Frischknecht, U., Hirschi, R., Pignatari, M., et al. 2016, *MNRAS*, 456, 1803
 Frischknecht, U., Hirschi, R., & Thielemann, F.-K. 2012, *A&A*, 538, 2
 Fulbright, J. P., McWilliam, A., & Rich, R. M. 2006, *ApJ*, 636, 821
 Fulbright, J. P., McWilliam, A., & Rich, R. M. 2007, *ApJ*, 661, 1152
 Gaia Collaboration, Brown, A. G. A., Vallenari, A., et al. 2018, *A&A*, 616, A1
 Gaia Collaboration, Prusti, T., de Bruijne, J. H. J., et al. 2016, *A&A*, 595, A1
 Gull, M., Frebel, A., Cain, M. G., et al. 2018, *ApJ*, 862, 174
 Hansen, T. T., Holmbeck, E. M., Beers, T. C., et al. 2018, *ApJ*, 858, 92
 Hayes, C. R., Majewski, S. R., Hasselquist, S., et al. 2018, *ApJL*, 859, L8
 Heger, A., & Woosley, S. E. 2002, *ApJ*, 567, 532
 Heger, A., & Woosley, S. E. 2010, *ApJ*, 724, 341
 Helmi, A., Babusiaux, C., Koppelman, H. H., et al. 2018, *Natur*, 563, 85
 Hinkle, K., Wallace, L., Livingston, W., et al. 2003, *The Future of Cool-Star Astrophysics*, in *Cambridge Workshop on Cool Stars, Stellar Systems, and the Sun12*, ed. A. Brown, G. M. Harper, & T. R. Ayres (Boulder, CO: Univ. Colorado), 851
 Holmbeck, E. M., Beers, T. C., Roederer, I. U., et al. 2018, *ApJ*, 859, 24
 Ivans, I. I., Sneden, C., James, C. R., et al. 2003, *ApJ*, 592, 906
 Iwamoto, K., Brachwitz, F., Nomoto, K., et al. 1999, *ApJS*, 125, 439
 Ji, A. P., Frebel, A., Simon, J. D., & Chiti, A. 2016, *ApJ*, 830, 93
 Kobayashi, C., Ishigaki, M. N., Tominaga, N., & Nomoto, K. 2014, *ApJ*, 785, 5
 Koppelman, H., Helmi, A., & Veljanoski, J. 2018, *ApJL*, 860, L11
 Kordopatis, G., Gilmore, G., Steinmetz, M., et al. 2013, *AJ*, 146, 134
 Kunder, A., Kordopatis, G., Steinmetz, M., et al. 2017, *AJ*, 153, 75
 Lanfranchi, G. A., Matteucci, F., & Cescutti, G. 2008, *A&A*, 481, 635
 Lattimer, J., & Schramm, D. 1974, *ApJL*, 192, L145
 Lind, K., Asplund, M., Barklem, P. S., & Belyaev, A. K. 2011, *A&A*, 528, 103
 Lippuner, J., Fernández, R., Roberts, L. F., et al. 2017, *MNRAS*, 472, 904
 Lovisi, L., Mucciarelli, A., Lanzoni, B., et al. 2012, *ApJ*, 754, 91
 Mashonkina, L., Sitnova, T. N., & Pakhomov, Y. V. 2016, *AsTL*, 42, 606
 Matijević, G., Chiappini, C., Grebel, E. K., et al. 2017, *A&A*, 603, 19
 McWilliam, A., Piro, A. L., Badenes, C., & Bravo, E. 2018, *ApJ*, 857, 97
 McWilliam, A., Wallerstein, G., & Mottini, M. 2013, *ApJ*, 778, 149
 Munari, U., Henden, A., Frigo, A., et al. 2014, *AJ*, 148, 81
 Nagasawa, D. Q., Marshall, J. L., Li, T. S., et al. 2018, *ApJ*, 852, 99
 Nishimura, N., Sawai, H., Takiwaki, T., Yamada, S., & Thielemann, F.-K. 2017, *ApJL*, 836, L21
 Nissen, P. E., & Schuster, W. J. 2010, *A&A*, 511, L10
 Nordlander, T., & Lind, K. 2017, *A&A*, 607, 75
 Placco, V. M., Beers, T. C., Santucci, R. M., et al. 2018, *ApJ*, 155, 256
 Placco, V. M., Frebel, A., Beers, T. C., & Stancliffe, R. J. 2014, *ApJ*, 797, 21
 Placco, V. M., Holmbeck, E. M., Frebel, A., et al. 2017, *ApJ*, 844, 18
 Ramírez, I., & Meléndez, J. 2005, *ApJ*, 626, 465
 Reddy, B. E., Lambert, D. L., & Prieto, C. A. 2006, *MNRAS*, 367, 1329
 Roederer, I. U., Cowan, J. J., Preston, G. W., et al. 2014a, *MNRAS*, 445, 2970
 Roederer, I. U., Hattori, K., & Valluri, M. 2018a, *AJ*, 156, 179
 Roederer, I. U., Mateo, M., Bailey, J. I., et al. 2016, *AJ*, 151, 82
 Roederer, I. U., Preston, G. W., Thompson, I. B., et al. 2014b, *AJ*, 147, 136
 Roederer, I. U., Sakari, C. M., Placco, V. M., et al. 2018b, *ApJ*, 865, 129
 Rossow, S., Korobkin, O., Arcones, A., Thielemann, F.-K., & Piran, T. 2014, *MNRAS*, 439, 744
 Sakari, C., Placco, V., Farrell, E., et al. 2018a, *ApJ*, 868, 110
 Sakari, C. M., Placco, V. M., Hansen, T., et al. 2018b, *ApJL*, 854, L20
 Schlafly, E. F., & Finkbeiner, D. P. 2011, *ApJ*, 737, 103
 Schuster, W. J., Beers, T. C., Michel, R., Nissen, P. E., & Garcia, G. 2004, *A&A*, 422, 527
 Shappee, B. J., Simon, J. D., Drout, M. R., et al. 2017, *Sci*, 358, 1574
 Shetrone, M., Venn, K., Tolstoy, E., et al. 2003, *AJ*, 125, 684
 Sneden, C. 1973, *ApJ*, 184, 839
 Sobeck, J. S., Kraft, R. P., Sneden, C., et al. 2011, *AJ*, 141, 175
 Steinmetz, M., & Müller, E. 1994, *A&A*, 281, 97
 Steinmetz, M., Zwitter, T., Siebert, A., et al. 2006, *AJ*, 132, 1645
 Stetson, P. B., & Pancino, E. 2008, *PASP*, 120, 1332
 Tailo, M., D'Antona, F., Milone, A. P., et al. 2017, *MNRAS*, 465, 1046
 Tody, D. 1986, *Proc. SPIE*, 627, 733
 Tody, D. 1993, in *ASP Conf. Ser. 52, Astronomical Data Analysis Software and Systems II*, ed. R. J. Hanisch, R. J. V. Brissenden, & J. Barnes (San Francisco, CA: ASP), 173
 Tolstoy, E., Hill, V., & Tosi, M. 2009, *ARA&A*, 47, 371
 Tsujimoto, T., & Nishimura, N. 2018, *ApJL*, 863, L27
 Valentini, M., Chiappini, C., Bossini, D., et al. 2018, arXiv:1808.08569
 Venn, K. A., Irwin, M., Shetrone, M. D., et al. 2004, *AJ*, 128, 1177
 Venn, K. A., Shetrone, M. D., Irwin, M. J., et al. 2012, *ApJ*, 751, 102
 Webster, D., Bland-Hawthorn, J., & Sutherland, R. 2015, *ApJL*, 799, L21
 Winteler, C., Käppeler, R., Perego, A., et al. 2012, *ApJL*, 750, L22
 Yong, D., Norris, J. E., Bessell, M. S., et al. 2013, *ApJ*, 762, 26